# Growth mechanism of chromia scales on a model Ni-30Cr alloy at high temperatures

Xian Huang, Sophie Bosonnet, Paul C M Fossati, Yves Wouters, Jérôme Aléon, Maximilien Verdier-Paoletti, François Jomard, Laure Martinelli

Corrosion Science 243 (2025) 112585

Contents lists available at ScienceDirect

Corrosion Science

journal homepage: www.elsevier.com/locate/corsci

# Growth mechanism of chromia scales on a model Ni-30Cr alloy at high temperatures

Xian Huang [a,b,*], Sophie Bosonnet [a], Paul C.M. Fossati [a], Laurence Latu-Romain [b], Yves Wouters [b], Jérôme Aléon [c], Maximilien Verdier-Paoletti [c], François Jomard [d], Laure Martinelli [a,**]

[a] Université Paris-Saclay, CEA, Service de recherche en Corrosion et Comportement des Matériaux, Gif Sur Yvette 91191, France
[b] Université Grenoble Alpes, CNRS, SIMaP, Grenoble 38000, France
[c] Institut de Minéralogie, Physique des Matériaux et Cosmochimie, Museum National d'Histoire Naturelle, UMR CNRS 7590, Sorbonne Université, Paris 75231, France
[d] Université Paris-Saclay, UVSQ, CNRS, GEMaC, Versailles 78000, France

ARTICLE INFO

*Keywords:*
Ni-Cr alloy
Chromia
TEM-ASTAR
SIMS and NanoSIMS
High temperature corrosion

ABSTRACT

Oxidation tests with markers and tracers were carried out to investigate the growth mechanism of chromia scale on a model Ni-30Cr alloy. The location of oriented grains characterized by TEM-ASRAR indicated that the scale grew predominantly outward at 800 and 900 °C. Experiments using $^{18}O$ and $^{54}Cr$ tracers confirmed a cationic transport via grain boundaries at these temperatures, using SIMS and NanoSIMS analyses. In the light of this and previous studies, we propose that the scales grow via diffusion of chromium vacancies at 900 °C and oxygen vacancies at 500 °C.

## 1. Introduction

Ni-based chromia-forming alloys are known as important structural materials for nuclear reactors of current [1] and future generations [2,3], thanks to their good corrosion resistance at high temperatures. This resistance comes from the formation of a protective chromia ($Cr_2O_3$) scale that grows slowly on the surface during the service of the alloys.

The growth of chromia scale follows in general a parabolic kinetic law [4,5]. In our previous studies [6,7], this kinetic behaviour was confirmed for a model Ni-30Cr alloy oxidized between 500 and 900 °C in argon, on which a single-phase chromia scale was formed. The parabolic kinetics suggests that the chromia growth rate is limited by diffusion processes [8], which can be Cr or O diffusion. In the literature, it was well reported that chromia growth on Ni-Cr alloys is controlled by diffusion of Cr at temperatures higher than 1000 °C over a wide range of oxygen partial pressures [9–12]. At an oxygen partial pressure of 1 atm, the same diffusive species was also identified for the oxidation of a Ni-Cr alloy [13] above 800 °C and for the oxidation of Cr metal [14,15] down to 400 °C. However, the diffusive species and the relevant diffusion paths are still not clear at temperatures lower than 1000 °C or oxygen partial pressures lower than 1 atm, due to the disagreement of results in the literature for the oxidation of Ni-Cr alloys [16–18] and Cr metal [19–24].

Experiments with markers [9–15,18,21–25] and tracers [16,17,19,20,26] are usually carried out to obtain insights on the diffusion mechanisms. In classical experiments with markers, platinum [9–11,13,14,25] and gold [12,15,18] assumed as inert markers are deposited usually by physical vapour deposition process on alloy surfaces to identify the growth direction of chromia scales. After oxidation tests, the presence of the markers at the oxide/alloy and environment/oxide interfaces indicates outward and inward growth via cationic and anionic diffusion, respectively. However, whether platinum or gold are truly inert is doubtful [27–30]. In a two-stage oxidation test of pure Cr at 800 °C [27], oxygen diffusion was detected in the presence of Pt markers, but not in another zone without markers. This catalytic effect of Pt markers on oxygen diffusion were also reported for the oxidation of Zr, Ni and Al at temperatures between 400 and 800 °C [28]. In the case of gold markers, it was reported that the oxidation kinetics of Ni at 700 °C is accelerated by the presence of gold markers [29]. Furthermore, the use of gold markers could also modify the semi-conductor character of the oxide layer, for instance from pure *n*-type to mixed *n*- and *p*- types for the chromia films formed on pure Cr at 800 °C [30]. The markers was found

* Corresponding author at: Université Paris-Saclay, CEA, Service de recherche en Corrosion et Comportement des Matériaux, Gif Sur Yvette 91191, France.
** Corresponding author.
*E-mail addresses:* xian-huang@outlook.com (X. Huang), laure.martinelli@cea.fr (L. Martinelli).

https://doi.org/10.1016/j.corsci.2024.112585
Received 24 June 2024; Received in revised form 8 November 2024; Accepted 16 November 2024
Available online 19 November 2024

scattered in the oxide layer, rather than remaining at the same depth, as they were non-homogeneously moved by the vertical and lateral growth of chromia during oxidation of a Ni-Cr alloy at 1000 °C [30].

Recently, a new marker technique was reported by Latu-Romain *et al.* [21–24]. Using TEM-ASTAR characterizations, they found that the oxide layer formed on pure Cr in a very short time (3 minutes at 900 °C) was composed of a single layer of nanometric grains oriented along the *c* axis of chromia. These grains were again observed in the oxide layer formed in a longer time, separating an inner layer of equiaxed grains and an outer layer of columnar grains, and they were considered as the one that grew in the early stage of oxidation. As a part of the oxide layer, the oriented grains were then considered as "natural markers" that indicated the location of initial oxide layer without perturbing the system, in contrast with *a priori* inert markers. With this technique, Latu-Romain *et al.* [21–24] identified the mixed outward and inward growth of chromia on pure Cr between 800 and 900 °C at very low oxygen partial pressures between $10^{-14}$ and $10^{-12}$ atm.

The second common method to identify diffusion mechanisms during chromia growth [16,17,19,20,26,31] is to use isotopic tracers in two-stage oxidation experiments [32,33]. In the experiments using $^{18}O$ tracers, samples are oxidized firstly in $^{18}O$-rich and then in $^{16}O$-rich (or firstly in $^{16}O$-rich and then in $^{18}O$-rich) atmospheres. If the 1st oxidation uses an $^{18}O$-rich atmosphere, during the 2nd oxidation in a $^{16}O$-rich atmosphere, one can basically distinguish three cases according to the $^{18}O$ profiles, illustrated in Fig. 1, depending on the diffusive specie and its diffusion pathway. Besides these situations, the possibility of O transport through cracks is also considered in the literature [32,33], but it is excluded here since no visible crack was observed in our oxide layers, as shown in our previous study [34]. $^{54}Cr$ tracers can also be used to investigate the diffusion process [17]. In such an experiment, a thin $^{54}Cr$ film is deposited on the sample surface before oxidation. Similarly to the experiments using $^{18}O$, there are three kinds of $^{54}Cr$ profiles, shown in Fig. 2, depending on the diffusion mechanism.

In tracer experiments [16,17,19,20,26], the isotope profiles are usually measured by secondary ion mass spectrometry (SIMS) or time-of-flight SIMS (ToF-SIMS) whose depth resolution is nanometric, but lateral resolution is micrometric. To obtain more accurate profiles, Falk-Windisch *et al.* [31] studied the growth of chromia on an Fe-20Cr alloy at 850 °C in humid air with O tracers not only by probing on surface using ToF-SIMS, but also by probing the transversal cross-section using nanoscale SIMS (NanoSIMS) that provide both nanometric depth and lateral resolution. NanoSIMS profiles suggested dominant cationic diffusion with secondary anionic diffusion via grain boundaries, while the ToF-SIMS profiles give a different conclusion, major anionic diffusion. The discrepancy was due to the roughness of surface and interfaces of oxide layer in the micrometric crater of the ToF-SIMS. The use of Nano-SIMS made it possible to highlight interpretation errors linked to the limitation of ToF-SIMS.

In this study, oxidation tests were carried out between 500 and 900 °C and at oxygen partial pressures about $10^{-5}$ atm using a model Ni-30Cr alloy, in order to better understand the growth mechanism of chromia scales which is still not clear at these temperatures and oxygen partial pressures. Many techniques were used in this study, including the advanced techniques TEM-ASTAR and NanoSIMS for the first time, to investigate the oxidation of Ni-30Cr alloys. Both $^{18}O$ and $^{54}Cr$ tracers were used to determine not only the diffusive species, but also its diffusion path. Once the growth direction is determined, the growth mechanism will be discussed using point defect models.

## 2. Method

The material and oxidation conditions were selected in order to form single-phase chromia layers on the alloy surfaces. The material used in this study was already described in detail in our previous published works [6,7]. The samples were made of a Ni-Cr alloy containing 69.85 wt% of Ni and 29.95 wt% of Cr and the two most common impurities were Si (450 ppm) and Fe (350 ppm). The plate samples were ground with SiC paper up to P500 grit before the oxidation tests.

To identify the growth direction using TEM-ASTAR characterization, oxidation tests were carried out with symmetric thermobalances using the protocol described in previous works [6,7]. Samples were oxidized in a mixed gas (0.25 $L{\cdot}h^{-1}$ of helium and 1 $L{\cdot}h^{-1}$ argon in each furnace) whose nominal oxygen partial pressure was measured at $5{\times}10^{-6}$ atm before oxidation. Five oxidation temperatures of 500, 600, 700, 800 and 900 °C were selected since the oxidation mechanism is not clear for this range of temperatures according to the literature. Oxidations at temperatures between 700 and 900 °C were carried out for 100 h, while the tests at 500 and 600 °C were extended to 1200 h and 300 h respectively in order to obtain measurable weight gains. Analyses with X-ray diffraction have confirmed the formation of single-phase chromia layers. Thermogravimetric analyses showed parabolic kinetics, indicating that the growth was controlled by a diffusion process under these oxidation conditions. These analyses were published in a previous study [7].

TEM-ASTAR is a crystal orientation mapping technique [35] using automated diffraction spot recognition by transmission electron microscopy (TEM). The transversal cross-section of thin lamellas of samples were prepared using focused ion beam and observed in a TEM (Jeol 2100 F) equipped with a field emission gun and an ASTAR system at the Grenoble Alpes University. Orientation mapping was performed with an electronic probe size of 1 nm, a step size of 2 nm and a precession of 1°.

To determine the growth direction separately, tests were carried out using $^{18}O$ or $^{54}Cr$ isotopic tracers coupled with *a priori* inert markers. In the tests conducted with $^{18}O$ tracers, Au markers were used. Samples were initially briefly oxidized in a gas containing only naturally

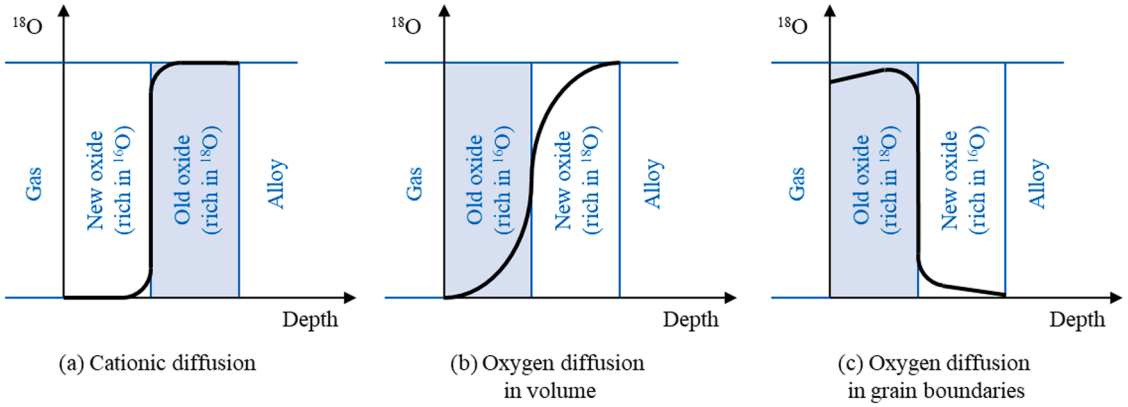


**Fig. 1.** Schematic illustration of $^{18}O$ concentration profiles for (a) cationic diffusion, (b) oxygen diffusion in volume and (c) at grain boundaries. The 1st oxidation (old oxides) takes place in an $^{18}O$-rich environment followed by a 2nd oxidation (new oxides) in an $^{16}O$-rich environment.

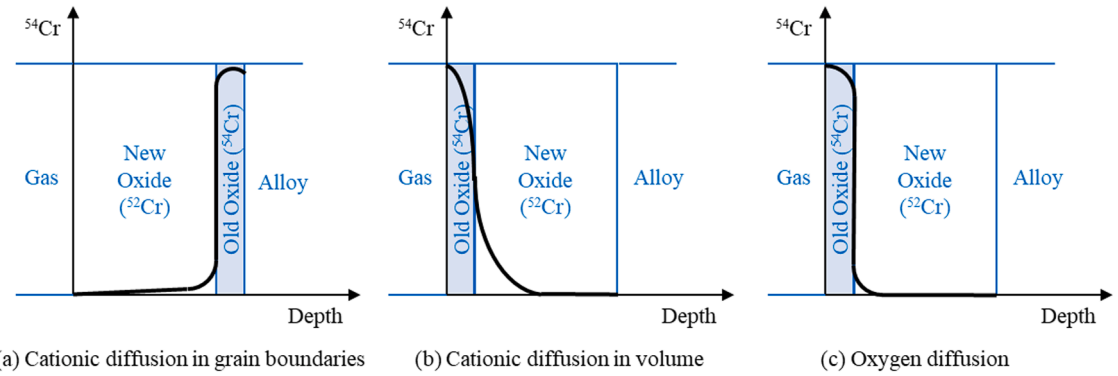


**Fig. 2.** Schematic illustration of $^{54}$Cr concentration profiles for cationic diffusion (a) at grain boundaries and (b) in volume and (c) oxygen diffusion.

abundant $^{18}$O (0.2 %). This pre-oxidation was aimed at forming a fine protective layer on the alloy surface before Au deposition to avoid Au diffusion into the alloy substrate. The durations of pre-oxidation are given in Table 1. Gold spots were deposited only on one of the two faces of samples in order to check if the Au deposition changed the resulting microstructure of the chromia scale. Since the results obtained on the two faces were similar, in the following, only the results of the face with gold markers will be presented. After Au deposition, the samples were oxidized in a gas with high $^{18}$O abundance compared to the natural level (1st oxidation) and then in a gas containing only naturally abundant $^{18}$O (2nd oxidation). The durations of the 1st and 2nd oxidation steps, compiled in Table 1, were selected based on the kinetic law [7] to ensure that the oxide thicknesses obtained during the two oxidations were comparable. Oxidation tests with $^{18}$O were performed either in a single-furnace thermobalance or in sealed quartz tube (Rhines pack [36]) in two separate furnaces. In both cases, $^{18}$O was introduced into the oxidizing environment without changing the nominal oxygen partial pressure of $2\times10^{-5}$ atm. For tests performed with $^{54}$Cr tracers, a very thin layer (15 nm) of pure $^{54}$Cr was deposited on one side of the samples before oxidation. One-stage oxidations were carried out in a single-furnace thermobalance in a mixture of argon and natural oxygen, with a nominal oxygen partial pressure of $2\times10^{-5}$ atm. More details of the oxidation tests with isotopic tracers are described in Appendix A.

Samples with isotopic tracers and inert markers were characterized by NanoSIMS and conventional SIMS. Both analyses used a Cs source with a positive charge to better ionize the O isotopes for tests with $^{18}$O tracers and an O source with a negative charge for Cr isotopes in the tests with $^{54}$Cr tracers. The optimal lateral resolution in NanoSIMS is in the order of 100 nm [37], which means that the thickness of the observed oxide scale should be at least about 1 μm for ionic imaging and profiling. The oxidations were therefore carried out at 800 and 900 °C in order to quickly form oxide layers with the appropriate thickness required to carry out NanoSIMS characterization. In the tests with $^{54}$Cr tracers, since the deposited $^{54}$Cr layer is too thin (15 nm) to be characterized by NanoSIMS, only SIMS analyses were considered.

**Table 1**
Oxidation durations and estimated thicknesses of oxide layer for tests with isotopic tracers. The nominal oxygen partial pressure is $2\times10^{-5}$ atm both in the thermobalance and in the Rhines pack. The thicknesses are estimated by mass gain and measured in an analytical balance.

| | | | Duration (h) | Thickness (μm) |
|---|---|---|---|---|
| 800 °C | $^{18}$O and Au markers in thermobalance | Pre-oxidation ($^{16}$O) | 0.67 | 0.07 |
| | | 1st oxidation ($^{18}$O) | 75 | 0.43 |
| | | 2nd oxidation ($^{16}$O) | 150 | 0.44 |
| | $^{54}$Cr | | 225 | 1.9 |
| 900 °C | $^{18}$O and Au markers in thermobalance | Pre-oxidation ($^{16}$O) | 0.33 | 0.2 |
| | | 1st oxidation ($^{18}$O) | 25 | 1.7 |
| | | 2nd oxidation ($^{16}$O) | 75 | 1.9 |
| | $^{18}$O and Au markers in Rhines pack | Pre-oxidation ($^{16}$O) | 0.33 | 0.4 |
| | | 1st oxidation ($^{18}$O) | 25 | 1.8 |
| | | 2nd oxidation ($^{16}$O) | 75 | 0.8 |
| | $^{54}$Cr | | 100 | 4.3 |

For the NanoSIMS analyses, isotopic and elemental cartography of the samples was performed with a CAMECA N50 NanoSIMS in the Institute of Mineralogy, Physics of Materials and Cosmochemistry at the National Museum of Natural History in France. Prior to analysis, the samples were mechanically cut in transversal cross-section and mounted in epoxy resin. The cross-section faces of the samples were polished up to the grade of 1 μm. To ensure conductivity of the surface, the polished sections were then coated with a nanometre-thin carbon layer. Five electron multipliers were dedicated to $^{16}$O, $^{18}$O, $^{52}$Cr, $^{52}$Cr$^{16}$O$_2$ and $^{197}$Au, which we measured in combined analysis mode. $^{52}$Cr and $^{52}$Cr$^{16}$O$_2$ images were used for controls, but the low ion yields resulted in the low ion counts. Hence, their images were discarded from the rest of the study. An entrance slit of 25 × 160 μm was used in combination with an aperture slit of 200 × 200 μm and an energy slit of 10 %. This configuration ensured a mass resolving power that enabled to discriminate any interferences from our masses of interest. Prior to mapping, samples were sputtered for 5 min using a current of 200 pA over an area of 30 × 30 μm to reach a stationary regime and to limit potential surface contaminations. The current was then reduced for measurement to 0.25 pA and the raster was limited to a central cleaned region of 5 × 5 and 10 × 10 μm for samples oxidized at 800 and 900 °C, respectively. Each acquisition had 256 × 256 pixels with a dwell time of 1 ms/px. Total acquisition times were of 40 min, 3 h and 40 min for samples oxidized at 800 °C in the thermobalance, at 900 °C in the thermobalance and at 900 °C in Rhines packs, respectively. The effective lateral resolution was estimated to be between 150 and 180 nm in the chosen measuring conditions, enabling for the discrimination of our interfaces. Finally, an electron gun was used to compensate for potential charge effects.

The cross-sections of samples that were characterized by NanoSIMS were also observed in scanning electron microscope (SEM) in secondary electrons (SE) and backscattered electrons (BSE) modes and characterized by energy dispersive X-ray spectrometry (EDX). A SEM (Zeiss Ultra 55) equipped with a field emission gun and an EDX microanalysis system (BRUKER) was used in this study.

For the SIMS analyses, the surfaces of the oxidized samples were characterized in conventional or checkerboard modes by a CAMECA IMS 7 f SIMS in the GEMaC laboratory of Paris-Saclay University in France. In conventional mode, the analysed area is limited by an optical gate

(mechanical aperture). Only the ions coming from the gated area are collected and recorded to avoid the crater edge effect. High count rates can be obtained in this mode. In checkerboard mode, ions from the whole sputtered surface are collected point by point for each scan. A stack of ions images is thus obtained for each analysed element. It is then possible to retrospectively extract signal from selected areas of the crater that are relatively smooth. In this mode, only ions from the selected smooth areas are counted, which helps reducing roughness effects. Samples with $^{18}O$ tracers were analysed in checkerboard mode, using an electron multiplier as a detector with a primary beam intensity about 50 nA. Samples with $^{54}Cr$ tracers were analysed in conventional mode, using a Faraday cage as a detector with a primary beam intensity about 150 nA. The raster size was 100 µm. After analysis, the crater depth was measured with a stylus profilometer (Dektak-8) to calculate the thickness of sputtered alloy by subtracting the oxide thickness estimated from oxidation weight gain. To convert the sputtering time to the profiling depth, the abrasion rates in the oxide layer and in the alloy were assumed to be constant and were calculated using the oxide thicknesses and the thickness of sputtered alloy, respectively.

## 3. Results

### 3.1. TEM-ASTAR

Samples of Ni-30Cr oxidized at temperatures between 500 and 900 °C under Ar ($5\times10^{-6}$ atm) in the thermobalance were characterized using the TEM-ASTAR technique to identify the preferential orientation of the oxide grains and possible natural markers. Fig. 3 shows ASTAR images illustrating the orientation and shape of the oxide grains. Orientations refer to the direction perpendicular to the oxide/alloy interface. The thin oxide layer formed at 500 °C (Fig. 3.a) mostly contains equiaxed chromia grains oriented along the *c* axis of chromia (direction [0001]). In the oxide layers formed at 600 and 700 °C (Fig. 3.b and Fig. 3.c), the oxide grains close to the oxide/alloy interface are rather equiaxed with diameters smaller than 50 nm and oriented along the [0001] direction compared to the columnar grains close to the gas/oxide interface with lengths between 100 and 400 nm. This phenomenon becomes even clearer for thick oxide layers formed at 800 and 900 °C (Fig. 3.d and Fig. 3.e).

According to the previous studies on the oxidation of pure Cr [21–23], the tiny grains oriented along the *c* axis should be formed at the early stage of oxidation and they could be considered as natural markers in the oxide layers. As they remain at the oxide/alloy interface after oxidation, one can consider that the growth of the layer of columnar grains formed between 600 and 900 °C is outward.

At 800 and 900 °C, the layer of grains oriented along the *c* axis is very thin compared to the layer of columnar grains, therefore outward growth is considered dominant. At 600 and 700 °C, the overall growth direction could be purely outward or mixed if the layer of oriented grains, whose thickness is not negligible compared to that of the layer of columnar grains, grow outwardly or inwardly, respectively. At 500 °C, since the oxide layer is mainly composed of the oriented grains, the growth direction is unknown and to be discussed in the next section.

### 3.2. NanoSIMS and SIMS

#### 3.2.1. $^{18}O$ tracers

To characterize the diffusing species and its diffusion path, tests using $^{18}O$ tracers and gold markers were carried out. As-ground samples were pre-oxidized briefly in a gas containing only naturally abundant $^{18}O$ before Au deposition. The as-deposited samples were oxidized initially in a gas with high $^{18}O$ compared to the natural level (1st

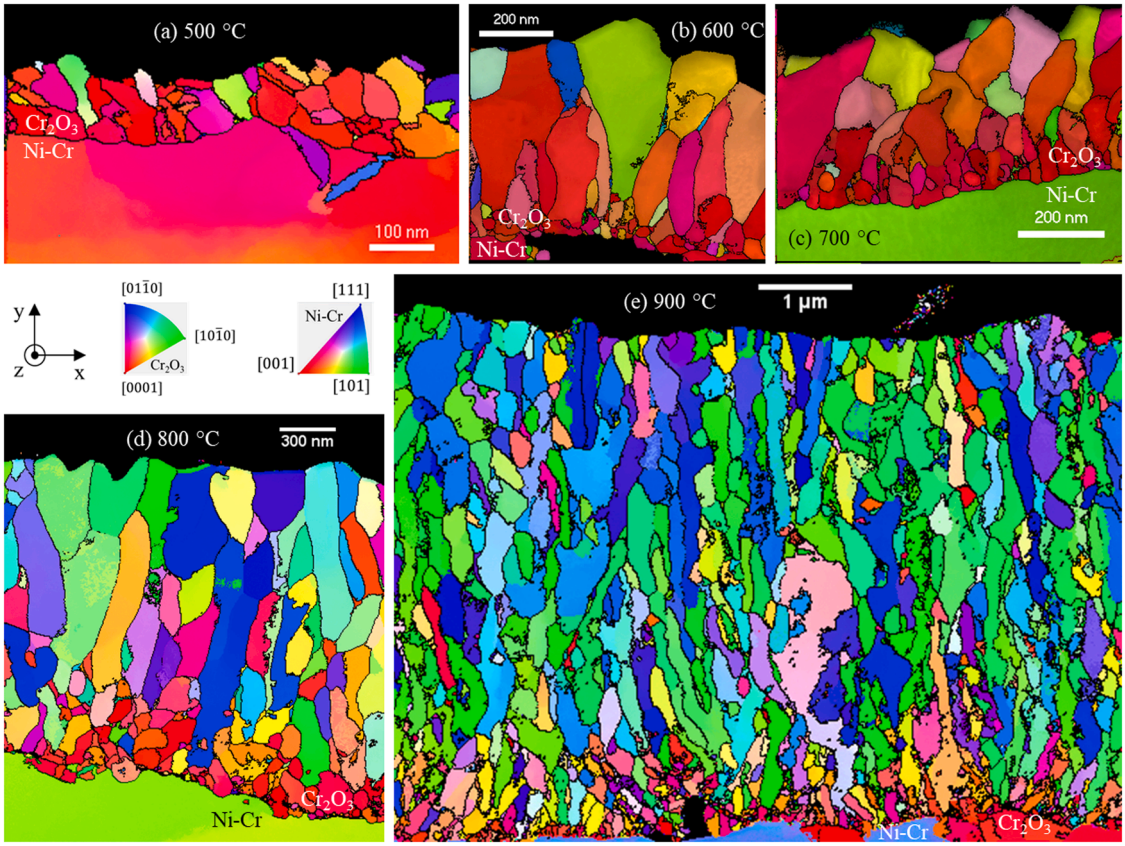


**Fig. 3.** TEM-ASTAR orientations maps along *y* direction (perpendicular to the oxide/alloy interface) combined with grain boundaries in black of Ni-30Cr oxidized (a) 1140 h at 500 °C, (b) 300 h at 600 °C, 100 h at (c) 700 °C, (d) 800 °C and (e) 900 °C in thermobalance under Ar (nominal oxygen partial pressure at $5\times10^{-6}$ atm).

oxidation) and then in a gas containing only naturally abundant $^{18}O$ (2nd oxidation).

Fig. 4 shows the BSE images of the cross-sectional view of the samples oxidized at 900 °C. Large pores (1 × 3 μm) that were regularly observed at the oxide/alloy interface in SEM, consistent to the TEM images previously published [34], probably resulted from the rapid growth of oxide scales. The sample oxidized in the thermobalance (Fig. 4.a) has a smoother oxide/alloy interface compared to the sample from the Rhines Pack (Fig. 4.b). Some protrusions, Ni-rich according to the EDX analysis, are observed in the oxide layer close to the oxide/alloy interface (Fig. 4.b) and they are not observed on the samples oxidized in thermobalance. The local thickness of the oxide scale is smaller than that formed in thermobalance at the same temperature with the same oxidation duration, compared to the average thicknesses estimated from weight gain (Table 1).

Fig. 5, Fig. 6 and Fig. 7 show the NanoSIMS maps of the samples oxidized at 800 and 900 °C in thermobalance and in Rhines Pack. The $^{16}O$ signal is observable throughout the oxide layer. For the sample oxidized at 900 °C in thermobalance, the $^{16}O$ signal (Fig. 6.a) is clearly divided into three zones: one close to the alloy and one close to the external interface with high count (red colour) and a central one with a relatively low count (yellow colour). The $^{18}O$ signal is observable in the middle of the oxide layer with a few spots at the inner interface. Close to the oxide/alloy interface, more $^{18}O$-rich grains are observed for the sample oxidized at 900 °C (Fig. 6.b) then in 800 °C in thermobalance. For the sample oxidized in Rhines Pack, the $^{18}O$-rich grains are not very visible at the oxide/alloy interface, but some traces of them can still be observed in the $^{18}O$ map (Fig. 7.b). No $^{197}Au$ signal is observed for sample oxidized at 800 °C. However, gold markers are observed on the $^{197}Au$ signal mapping for the samples oxidized at 900 °C in thermobalance (Fig. 6.c) and in Rhines Pack (Fig. 7.c) and they are dispersed in the oxide layer formed at 900 °C in Rhines Pack (Fig. 7.c).

Fig. 8 presents the NanoSIMS signals overlapped on the SEM-SE images. $^{18}O$ (in green) is present in the middle of the oxide layer (band) and to a lesser extent at the oxide/alloy interface (islets), whereas $^{16}O$ (in blue) is particularly present at the proximity of internal and external interfaces.

Fig. 9.a, Fig. 10.a and Fig. 11.a show the profiles of oxygen ($^{16}O$, $^{18}O$ and $^{16}O+^{18}O$) measured along the red arrow drawn in Fig. 8. For each sample, several profiling at different places were carried out and the obtained profiles have similar shapes. The position of the gas/oxide interface was determined by the half-maximum of the total O (i.e., $^{16}O+^{18}O$) profile and set to zero. Since the count in the alloy is not zero, the position of the oxide/alloy interface was identified by the midpoint between the oxide and the alloy levels. The total O profile near the gas/oxide interface is gradual due to a topographic effect probably resulting from the shrinkage of the resin during solidification. For the sample oxidized at 800 °C in thermobalance, the $^{16}O$ part between the $^{18}O$ and alloy parts is invisible in the profiles because of its small thickness.

The $^{18}O$ content estimated by the fraction of count of $^{18}O$ over that of total O, is shown in Fig. 9.b, Fig. 10.b and Fig. 11.b. The position at the half-maximum of this profile was considered as the interface between oxides rich in $^{16}O$ and $^{18}O$. The profiles are sharp at the $^{16}O/^{18}O$ interface, with a transition length (from 16 % to 84 % of the maximum) close to the lateral resolution (150 ~ 180 nm), indicating the absence of oxygen diffusion between these oxides. For the sample oxidized in 900 °C in thermobalance, the $^{18}O$ peak close to the oxide/alloy interface in Fig. 10.a corresponds to one of these grains crossed by the red arrow in Fig. 8.b.

For the sample oxidized in 900 °C in Rhines Pack, the ratio $^{18}O/(^{16}O+^{18}O)$ reaches the natural level (0.002 [38]) in the $^{16}O$-rich parts. In the $^{18}O$-rich part, the level of $^{18}O/(^{16}O+^{18}O)$ is much lower compared to the oxidation in the thermobalance because the $^{18}O$ isotope in the Rhines pack comes from the reduction of CuO powder which is formed by oxidation of $Cu_2O$ in $^{18}O_2$ (so maximal 50 at% of $^{18}O$ in CuO).

The gas/$^{16}O/^{18}O/^{16}O$/alloy sequence observed in the overlapped images (Fig. 8) is the same as the oxidation sequence. Moreover, the $^{16}O/^{18}O$ interface is sharp (Fig. 9.b, Fig. 10.b and Fig. 11.b), suggesting that outward growth by cationic diffusion is dominant during oxidation according to the principles of two-stage oxidation experiments (Fig. 1.a). Therefore, the thin $^{16}O$-rich part close to the internal interface is the oxide layer formed by the brief pre-oxidation in $^{16}O$. The $^{18}O$-rich layer and the thick $^{16}O$-rich layer near the external interface are formed during the first oxidation in $^{18}O$ and the second oxidation in $^{16}O$, respectively. For the samples oxidized in thermobalance, islets rich in $^{18}O$ from the first oxidation are located between the alloy and the thin oxide layer formed during the pre-oxidation in $^{16}O$. The observation of these isolated oxide grains implies a minor inward growth by oxygen diffusion along grain boundaries (see Fig. 1.c but note that now we consider the oxidation firstly in $^{16}O$ during the "pre-oxidation" and then in $^{18}O$ during the "1st oxidation"). Fig. 12 illustrates the corresponding structure of layers.

To compare with the NanoSIMS analysis, the same samples in $^{18}O$ tracer experiments are analysed by SIMS with the $Cs^+$ source to measure oxygen profiles in negative secondary ions mode. Measurements are performed in checkerboard mode [39], in which the data could be extracted from a selected zone that is relatively smooth in the sputtered area to avoid the roughness effect. The sputtering time needed to reach the oxide/alloy interface is determined by the half-maximum of the total oxygen signal ($^{16}O + ^{18}O$). Sputtering time can be converted linearly to the depth in the oxide and in the alloy parts by considering that the depths at the oxide/alloy interface and at the end correspond to the oxide thickness (estimated by weight gain of alloy after oxidation) and the crater depth, respectively.

Fig. 13 shows the $^{18}O/(^{16}O+^{18}O)$ profiles, calculated by the count ratio of $^{18}O$ to total O from SIMS measurements. In all cases, the $^{18}O$-rich part of the oxide layer is close to the internal interface and the $^{18}O$-depleted part is close to the external interface.

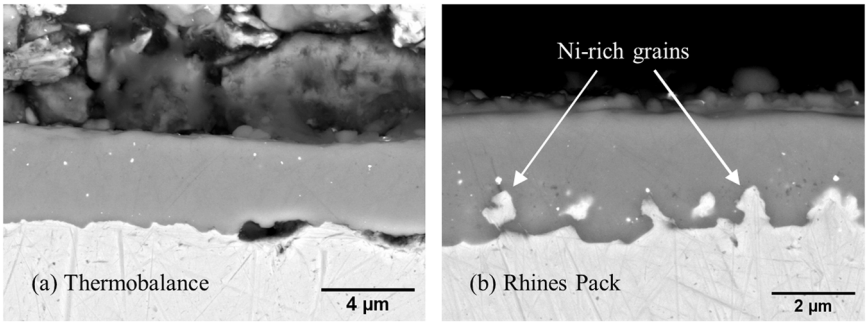


**Fig. 4.** SEM-BSE images of Ni-30Cr with gold markers oxidized 100 h at 900 °C (a) in thermobalance and (b) in Rhines Pack (nominal oxygen partial pressure at $2\times10^{-5}$ atm).

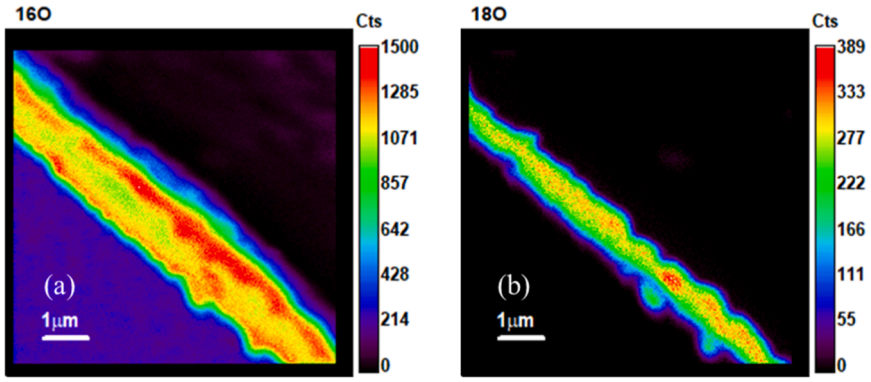


**Fig. 5.** NanoSIMS elemental maps of (a) $^{16}O$ and (b) $^{18}O$ of Ni-30Cr with gold markers oxidized 225 h (0.67 h in $^{16}O$, 75 h in $^{18}O$ and 150 h in $^{16}O$) at 800 °C in thermobalance under Ar (nominal oxygen partial pressure at $2\times10^{-5}$ atm).

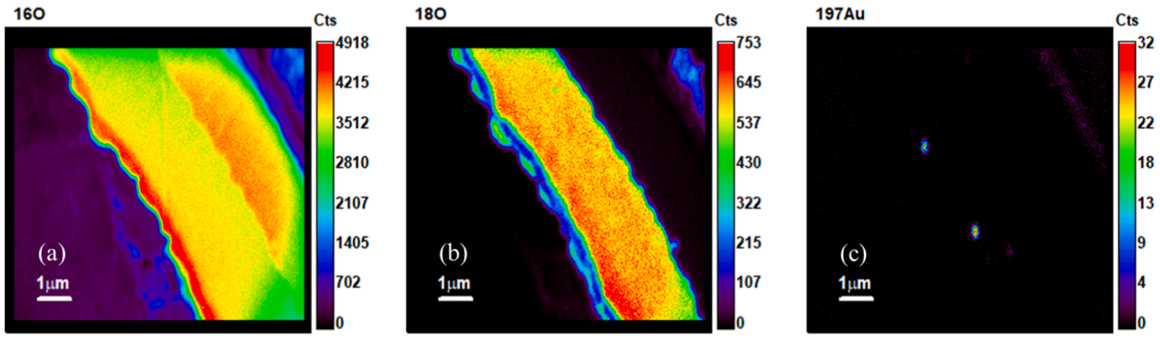


**Fig. 6.** NanoSIMS elemental maps of (a) $^{16}O$, (b) $^{18}O$ and (c) $^{197}Au$ of Ni-30Cr with gold markers oxidized 100 h (0.33 h in $^{16}O$, 25 h in $^{18}O$ and 75 h in $^{16}O$) at 900 °C in thermobalance under Ar (nominal oxygen partial pressure at $2\times10^{-5}$ atm).

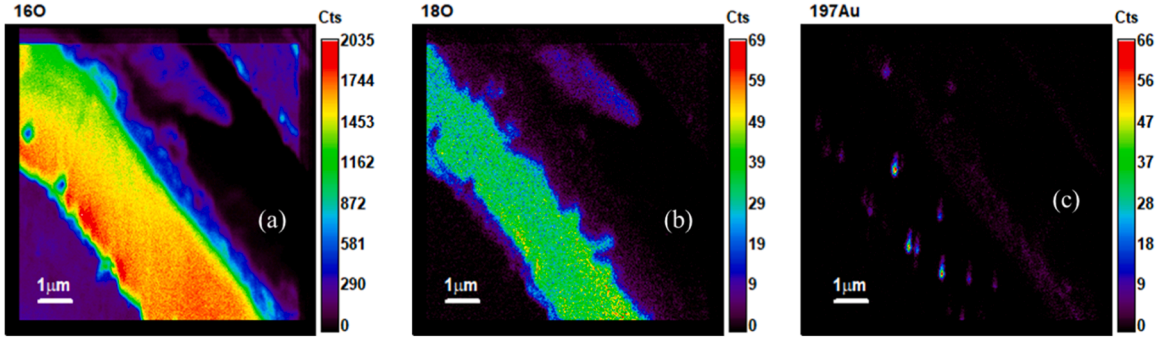


**Fig. 7.** NanoSIMS elemental maps of (a) $^{16}O$, (b) $^{18}O$ and (c) $^{197}Au$ of Ni-30Cr with gold markers oxidized 100 h (0.33 h in $^{16}O$, 25 h in $^{18}O$ and 75 h in $^{16}O$) at 900 °C in Rhines Pack (nominal oxygen partial pressure at $2\times10^{-5}$ atm).

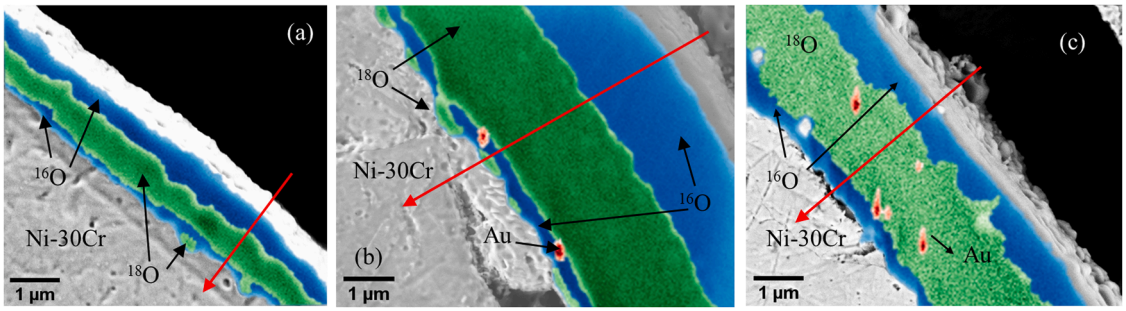


**Fig. 8.** NanoSIMS signals overlapped on the SEM-SE images of Ni-30Cr with gold markers oxidized (a) at 800 °C in thermobalance, (b) at 900 °C in thermobalance and (c) at 900 °C in Rhines Pack under Ar (nominal oxygen partial pressure at $2\times10^{-5}$ atm).

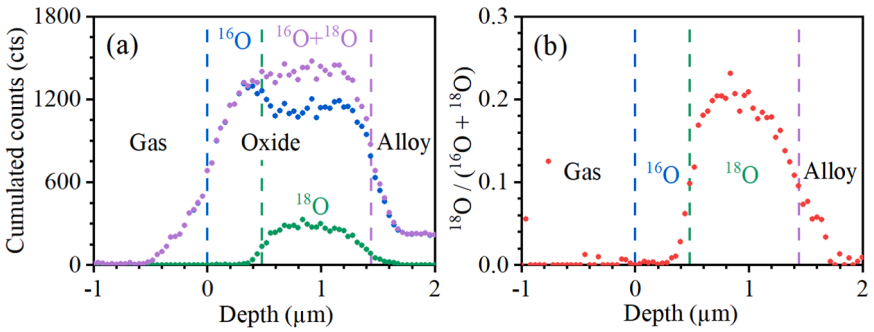


**Fig. 9.** (a) NanoSIMS oxygen profiles and (b) $^{18}O/(^{16}O+^{18}O)$ profile of Ni-30Cr oxidized 225 h (0.67 h in $^{16}O$, 75 h in $^{18}O$ and 150 h in $^{16}O$) at 800 °C in thermobalance under Ar (nominal oxygen partial pressure at $2\times10^{-5}$ atm). The profile is measured along the line marked by the red arrow in the SEM-SE image combined with NanoSIMS elemental maps. $^{16}O$ and $^{18}O$ maps and profiles are marked in blue and green, respectively. Total O profile ($^{16}O + {}^{18}O$) in purple. Gas/$^{16}O$, $^{16}O/^{18}O$ and oxide/alloy interfaces are marked by vertical dashed lines in blue, green and purple, respectively.

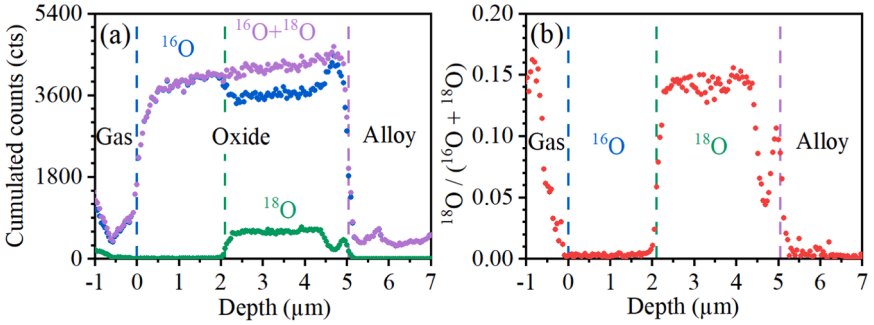


**Fig. 10.** (a) NanoSIMS oxygen profiles and (b) $^{18}O/(^{16}O+^{18}O)$ profile of Ni-30Cr oxidized 100 h (0.33 h in $^{16}O$, 25 h in $^{18}O$ and 75 h in $^{16}O$) at 900 °C in thermobalance under Ar (nominal oxygen partial pressure at $2\times10^{-5}$ atm). The profile is measured along the line marked by the red arrow in the SEM-SE image combined with NanoSIMS elemental maps. $^{16}O$ and $^{18}O$ maps and profiles are marked in blue and green, respectively. Total O profile ($^{16}O + {}^{18}O$) in purple. Gas/$^{16}O$, $^{16}O/^{18}O$ and oxide/alloy interfaces are marked by vertical dashed lines in blue, green and purple, respectively.

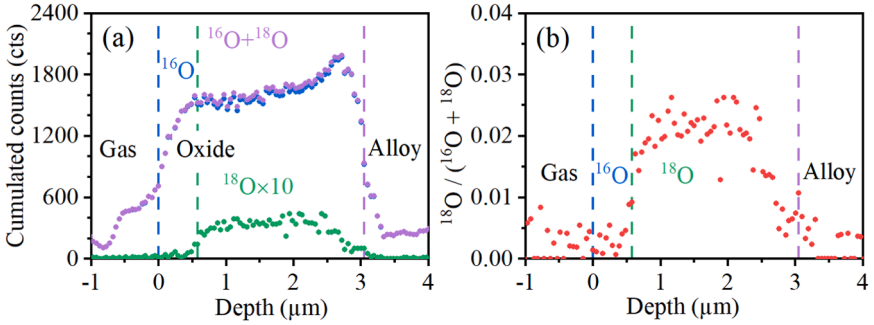


**Fig. 11.** (a) NanoSIMS oxygen profiles and (b) $^{18}O/(^{16}O+^{18}O)$ profile of Ni-30Cr oxidized 100 h (0.33 h in $^{16}O$, 25 h in $^{18}O$ and 75 h in $^{16}O$) at 900 °C in Rhines pack (nominal oxygen partial pressure at $2\times10^{-5}$ atm). The profile is measured along the line marked by the red arrow in the SEM-SE image combined with NanoSIMS elemental maps. $^{16}O$ and $^{18}O$ maps and profiles are marked in blue and green, respectively. Total O profile ($^{16}O + {}^{18}O$) in purple. Gas/$^{16}O$, $^{16}O/^{18}O$ and oxide/alloy interfaces are marked by vertical dashed lines in blue, green and purple, respectively.

### 3.2.2. *$^{54}Cr$ tracers*

Tracer experiments with $^{18}O$ suggested that cationic diffusion was dominant at 800 and 900 °C. To study the associated diffusion path, tracer experiments with $^{54}Cr$ were carried out based on the principle of two-stage oxidation experiments.

The oxidized samples were analysed by SIMS in conventional mode with an $O_2^+$ source to obtain good signals for the Cr isotopes ($^{50}Cr$, $^{52}Cr$, $^{53}Cr$ and $^{54}Cr$) in positive secondary ions mode. Before analysing the samples, a thin gold layer was deposited on the surface to avoid a charge evacuation problem, which could abnormally increase the count rates during the analysis. The total Cr signal ($^{50}Cr + {}^{52}Cr + {}^{53}Cr + {}^{54}Cr$) was used to determine the sputtering time needed to reach the oxide/alloy interface in order to convert sputtering time to depth as for O profiles.

Fig. 14 shows the $^{54}Cr$ / ($^{50}Cr + {}^{52}Cr + {}^{53}Cr + {}^{54}Cr$) profiles, estimated by the count ratio of the $^{54}Cr$ signal to the total Cr signal from the SIMS profiles. Peaks are observed near the internal interface, corresponding to the case in Fig. 2.a. This suggests that the dominant Cr diffusion, identified by $^{18}O$ tracer experiments, occurs via grain boundaries. The peaks of $^{54}Cr$ are centred on the oxide/alloy interface with large widths, implying a diffusion of $^{54}Cr$ both towards the oxide layer and the substrate.

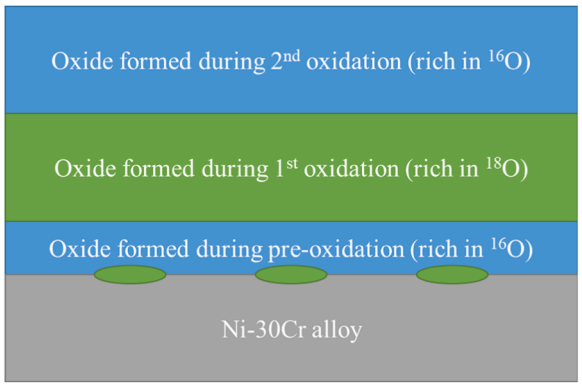


**Fig. 12.** Structure of oxide layers formed at 800 and 900 °C in thermobalance.

## 4. Discussion

### 4.1. Growth direction

Oxidation tests were carried out in thermobalance and in Rhines pack at 900 °C. The Rhines pack was heated separately by a furnace on each side and during oxidation tests, water drops were observed in the middle of the sealed tube between the two furnaces, suggesting that the corrosive environment contains water vapour. The existence of water vapour may influence the oxidation kinetics and the microstructure of oxide scales [40,41]. In a recent study, it was reported that oxidation of a Si-free alloy under water vapour can form Si-doped oxide scales [42]. The Ni-rich protrusions observed in the thin oxide scale formed in Rhines pack (Fig. 4) may result from the difference of the corrosive environments between tests in thermobalance and in Rhines pack. The effect of water vapour may be investigated in further studies and the present work focused on the investigation of the diffusing species.

Samples oxidized in $^{18}O$ at 800 and 900 °C were characterized both

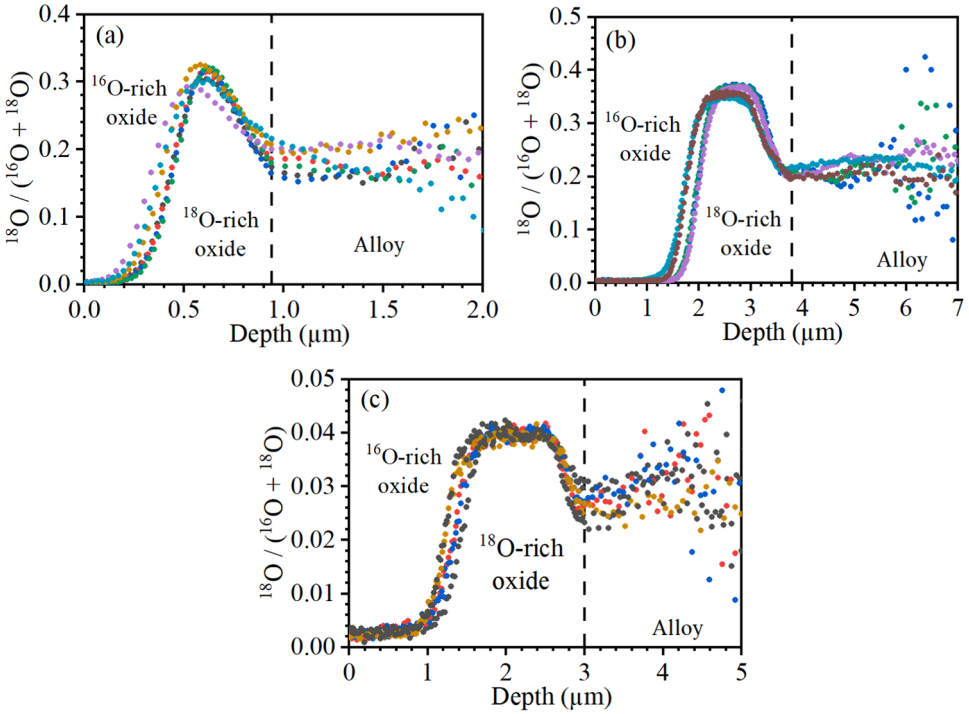


**Fig. 13.** $^{18}O/(^{16}O+^{18}O)$ ratio calculated from SIMS profiles performed on Ni-30Cr samples oxidized (a) 225 h at 800 °C in thermobalance, (b) 100 h at 900 °C in thermobalance and (c) 100 h at 900 °C in Rhines pack with nominal oxygen partial pressure at $2\times10^{-5}$ atm. Vertical dashed lines mark the oxide/alloy interfaces. For each sample, profiles measured at different zones are marked by different colours.

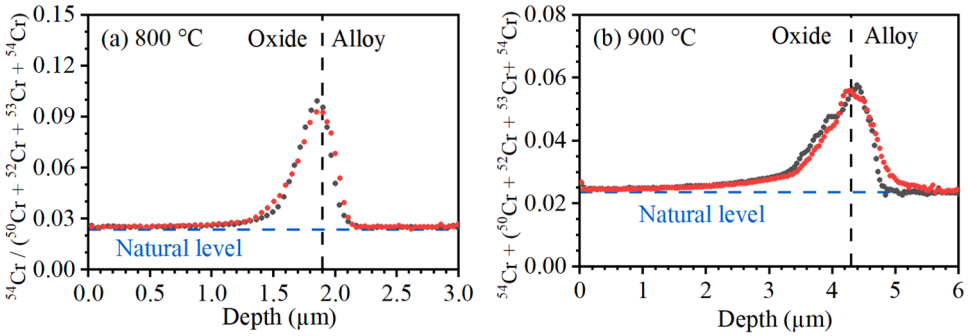


**Fig. 14.** $^{54}Cr$ / ($^{50}Cr$ + $^{52}Cr$ + $^{53}Cr$ + $^{54}Cr$) profile of Ni-30Cr oxidized (a) 225 h at 800 °C and (b) 100 h at 900 °C in thermobalance under Ar (nominal oxygen partial pressure at $2\times10^{-5}$ atm). The oxide/alloy interface is marked by the vertical dashed black lines. The natural level [38] is marked by the horizontal dashed blue lines.

by SIMS and NanoSIMS techniques. The $^{18}O/(^{16}O+^{18}O)$ profiles at the $^{16}O/^{18}O$ interface are less sharp for those measured by SIMS (Fig. 13) than those measured by NanoSIMS (Fig. 9, Fig. 10 and Fig. 11), which may lead to misunderstanding of the diffusing element and its diffusion pathway. This phenomenon is probably due to a roughness effect, as reported by Falk-Windisch *et al.* [31], but their relation is still not clear. The roughness that the samples exhibit on the surface, the $^{16}O/^{18}O$ interface and the SIMS crater could come from the roughness of the oxide surface, accentuated during sputtering. The mixing-roughness-information depth model [43] describes the effects of atomic mixture, information depth and roughness on a SIMS profile. According to this model, when the effects of atomic mixture and information depth are negligible, the SIMS profile of a weakly diffusing species across a rough interface can have the same shape as the one of a strongly diffusing species across a flat interface. If we have $\sigma > \sqrt{2Dt}$ where $\sigma$ is the roughness, $D$ the diffusion coefficient and $t$ the diffusion time, the influence of roughness on the profile will be more important than that of volume diffusion, which is the case in the present work. The model that discusses the roughness effect on a SIMS profile is provided in Appendix B.

Two types of marker technique were applied in order to determine chromia growth direction. In inert marker experiments, the gold markers observed in NanoSIMS are located at the interface between the layers formed during the pre-oxidation in $^{16}O$ and the first oxidation in $^{18}O$ for the sample oxidized at 900 °C in thermobalance, but they are scattered for the sample oxidized in Rhines Pack. The SEM-EDX analysis (Fig. 1S to Fig. 3S in supporting information) shows that for all samples, the positions of the gold markers are scattered inside the layer. These results reveal the instability of inert markers in oxidation tests between 800 and 900 °C, as suggested in some recent studies [27–30]. Using the textured chromia grains near the oxide/alloy interface characterized in TEM-ASTAR, which acts as natural markers, a major outward growth is identified for the chromia scales formed at 800 and 900 °C. This result is in agreement with that of the robust NanoSIMS analyses in the $^{18}O$ tracer experiments, confirming the interest of the concept of natural markers.

Fig. 15 summarizes the chromia growth direction identified in this study and reported in the literature for different oxidation environments. The results in the literature suggest that the growth is outward at temperatures higher than 1000 °C or at an oxygen partial pressure of 1 atm. At lower temperatures or oxygen partial pressures, the results determined by inter marker and SIMS characterizations in the literature were not in agreement. In this study, the outward growth at 800 and 900 °C identified by both TEM-ASTAR and NanoSIMS characterizations confirm the literature results obtained at higher temperatures and oxygen partial pressures.

At temperatures lower than 800 °C, inward growth via anionic diffusion was identified by gold markers on Ni-30Cr [18] and by $^{18}O$ tracers on pure Cr [20], indicating a possible change in growth direction. In this study, the TEM-ASTAR characterizations show that the thickness of the textured layers becomes significant compared to the total oxide layers as the temperatures for samples oxidized between 500 and 700 °C (Fig. 3). Therefore, the growth direction of the total oxide layer depends both on the outward-growing untextured layer and on the textured layer whose growth direction is to be discussed.

On the oxide film formed at 800 and 900 °C, grains rich in $^{18}O$, indicating a minor anionic diffusion via grain boundaries, are observed near the internal interface where the grains textured along the *c* axis of chromia are located. Fig. 16 shows a comparison of the $^{18}O$-rich grains and the textured grains at 900 °C, locating in the same layer whose thickness is about 300 nm. If the $^{18}O$-rich grains are a part of the textured grains, then the textured grains could be considered growing at least partially by anionic diffusion. At the lower temperatures between 500 and 700 °C, the textured grains are also observed, suggesting that the oxide films could also grow at least partially by anionic diffusion at these temperatures.

### 4.2. *Diffusing defects that drive the oxide growth*

The growth of continuous oxide films at high temperatures can be explained by the point defect model developed by Wagner [8,44]. According to this model, the chromia growth is limited by the diffusion of its intrinsic point defects [6,12,20–24]. In the present work, major chromium and minor oxygen diffusion, at grain boundaries rather than in volume, is identified for chromia growth at 800 and 900 °C. However, it is still a subject to discuss if the point defect model can be used to describe the growth via grain boundary diffusion [45]. Atkinson and Taylor [46] reported different diffusion coefficients at grain boundaries under different oxygen partial pressures measured in high-purity NiO, suggesting that enhanced diffusivity at grain boundaries relied on nearby Ni vacancies, whose concentration was controlled by the oxygen partial pressure. Indeed, the presence of interfaces between two grains with different orientations can induce lattice distortions nearby in the adjacent grains and provide new pathways that do not exist in the volume of the crystal lattice for atom diffusion. This generally facilitates the formation and diffusion of point defects in the affected zone, as shown by the studies in iron [47–49] and oxides [50,51]. With this atomistic model, one could consider that the chromia growth is carried out by the diffusion of point defects in grain boundary affected zones.

In the Wagner model, oxidation kinetics depends both on the diffusion coefficient of the defects that drives oxide growth and the difference of their concentrations at the interfaces [8]. Besides, the diffusion coefficient of an element via a kind of point defects is proportional to the mobility of that defect and its concentration [52]. Even though the defects ensuring the transport of matter during the oxide growth are not necessarily the dominant or the most mobile defects, the defect chemistry of chromia can still provide some insights on the growth

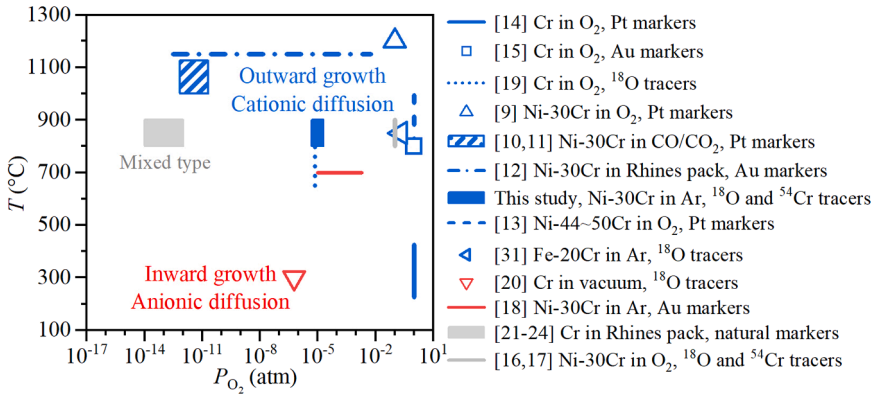


**Fig. 15.** Graph of chromia growth direction identified by marker or tracer experiments [9–24,31]. Outward, inward and mixed types are marked in blue, red and grey, respectively.

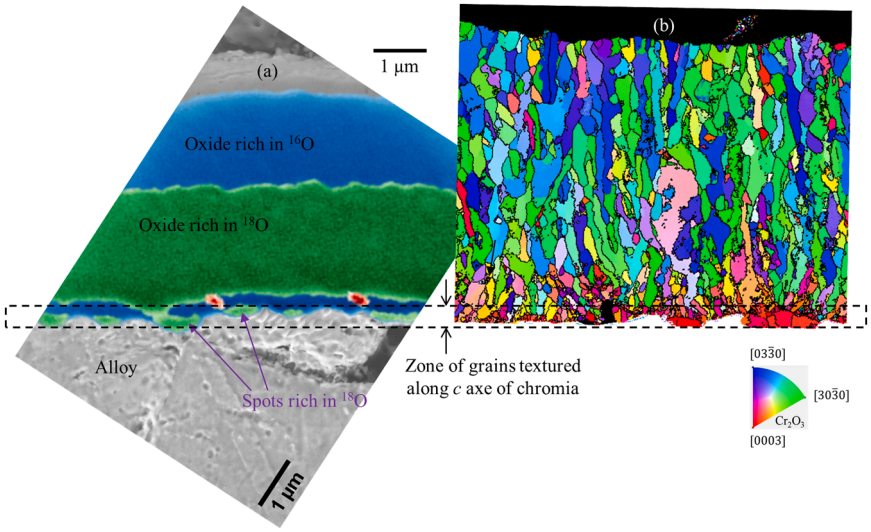


**Fig. 16.** (a) $^{18}O$-rich spots by NanoSIMS mapping and (b) grains textured along the *c* axis of chromia by TEM-ASTAR mapping for Ni-30Cr oxidized 100 h at 900 °C. The white part in the TEM-ASTAR mapping is the metallic substrate. The scale is the same for both images.

mechanism.

Defect formation can be influenced by the presence of grain boundaries [51], but to the best of our knowledge, the formation of point defects near $Cr_2O_3$ grain boundaries has not been studied. If the formation energies of defects are influenced in a comparable way by the presence of nearby grain boundaries, then the dominant defects at grain boundaries are also dominant in the bulk. The information about dominant point defects could be gathered from the semiconducting properties of the oxide films. Fig. 17 shows four situations that associate growth direction, semiconductor character and nature of the dominant point defect. O interstitials are included here even though their presence in oxide is sometimes doubtful due to their large ionic radius [53].

In our previous study [7], it was reported that one *n*-type semiconductor character was identified in chromia formed at 500 °C, two characters (*n*- and insulating-types) between 600 and 800 °C and another two characters (*n*- and *p*-types) at 900 °C. According to the Brouwer diagram [54], the defects with positive charges (oxygen vacancies and chromium interstitials) are more favourable at low oxygen partial pressure, resulting in an *n*-type semiconductor. Thus, for chromia formed at 900 °C containing two characters, the *n*-type can be considered near the internal interface and the *p*-type semiconductor character is close to the external gas/oxide interface. Table 2 summarizes the experimental results for chromia oxide scales formed on Ni-30Cr at 500 and 900 °C at oxygen partial pressures between $5\times10^{-6}$ and $2\times10^{-5}$ atm.

**Table 2**
Results of tracer experiments, TEM-ASTAR and PEC characterizations [34] for chromia oxide scales formed on Ni-30Cr at 500 and 900 °C at an oxygen partial pressure from $5\times10^{-6}$ to $2\times10^{-5}$ atm.

| Temperature | Tracers | TEM-ASTAR | PEC |
|---|---|---|---|
| 900 °C | Majorly cationic | Outward grains | *p*-type near external interface |
| | Minorly anionic | Textured grains near internal interface | *n*-type near internal interface |
| 500 °C | Partially or totally anionic | Textured grains | *n*-type |

The growth of chromia at 900 °C is majorly cationic but it is not clear whether the scale is mostly *p*-type. Fig. 18 illustrates five possible configurations combining the microstructure and the semiconductor character in the $Cr_2O_3$ oxide layer formed in 900 °C. In a previous study using DFT simulations to calculate defect formation energies in bulk chromia [55], it was found that vacancies are always more favourable than interstitials in the 400–1200 °C temperature range. If the *n*-type part in the oxide film formed at 900 °C is not negligible (Fig. 18.a or Fig. 18.b), then the outward growth of oxide film depends at least partially on the

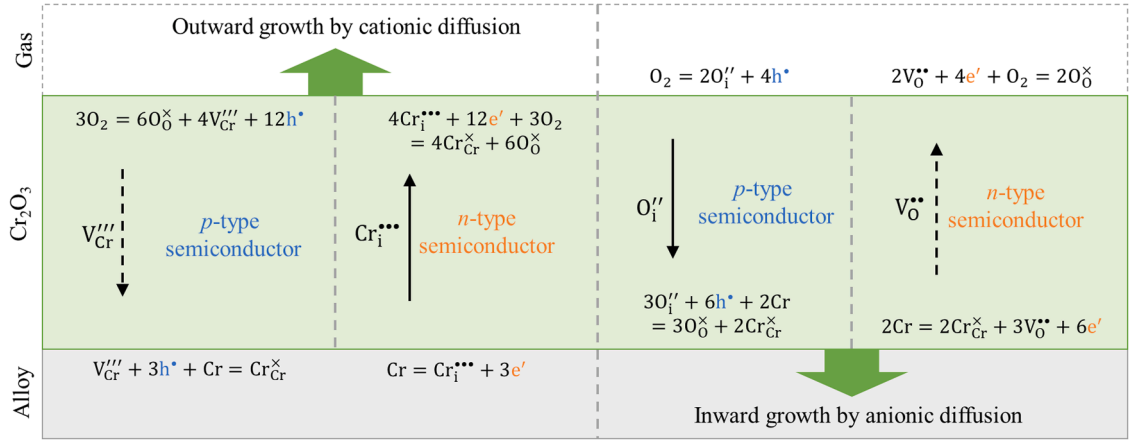


**Fig. 17.** Growth direction and semiconductor character associated to defects that drive the growth of chromia.

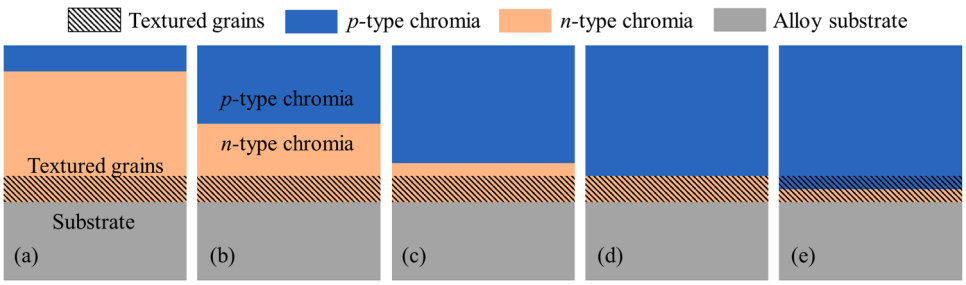


**Fig. 18.** Contributions of semiconductor characters of chromia oxide film formed at 900 °C: (a) mostly *n*-type, (b) comparable *n*- and *p*- types, (c) mostly *p*-type with a part of external grains contain *n*-type, (d) *p*-type for the whole external grain layer and *n*-type for the whole textured layer near internal interface and (e) the textured layer near the internal interface containing both *n*- and *p*- types. *n*- and *p*-type semiconductors are marked in orange and blue, respectively. The alloy substrate in grey. The hatched area is the textured grains along the *c*-axis of chromia near internal surface.

chromium interstitials, which is not consistent with what the DFT study suggests [55]. In other words, it is suggested that the oxide scale grows via the diffusion of chromium vacancies at 900 °C (Fig. 18.c, Fig. 18.d or Fig. 18.e).

The experimental results (Table 2) show that the oxide layer of chromia formed at 500 °C is *n*-type but the dominant mobile element or growth direction is not certain. If the film grows majorly by cationic diffusion at 500 °C, then chromium interstitials should be responsible for the growth (Fig. 17), which is again in disagreement with the DFT study [55] suggesting that vacancies are more favourable than interstitials. Therefore, it can be assumed that the growth of the textured grains is driven by the diffusion of oxygen vacancies at 500 °C.

Here we suggest a comprehensive picture that relates all insights: the grains textured along the *c* axis of chromia always observed at any temperature between 500 and 900 °C grow by the diffusion of oxygen vacancies. The grains above grow by the diffusion of chromium vacancies. Fig. 19 illustrates this proposal in a diagram. At an oxygen partial pressure between $5\times10^{-6}$ and $2\times10^{-5}$ atm and at low temperatures like 500 °C, the outward growth via chromium vacancies is negligible so that only the textured grains with *n*-type semiconductor character are observed. As the temperature increases, diffusion via chromium vacancies becomes comparable, even dominant at 900 °C, leading to a major outward growth.

## 5. Conclusion

Oxidation tests with markers and tracers were carried out in this study, followed by characterizations using advanced techniques, to provide insights on the growth mechanism of chromia oxide layer on a model Ni-30Cr alloy.

According to the TEM-ASTAR characterizations, chromia formed at 500 °C under Ar ($5\times10^{-6}$ atm) contains mostly grains oriented along the *c* axis of chromia, which are close to the oxide/alloy interfaces and play the role of markers in the oxide layers formed between 600 and 900 °C. Large columnar grains are close to the gas/oxide interfaces in the chromia layers formed above 500 °C, especially at 800 and 900 °C, suggesting a dominant outward growth at 800 and 900 °C.

NanoSIMS imaging of samples sequentially oxidized in Ar ($2\times10^{-5}$ atm) rich in $^{16}O$, $^{18}O$ and then in $^{16}O$ at 800 and 900 °C shows a succession of gas/$^{16}O$/$^{18}O$/$^{16}O$/alloy layers that corresponds to the oxidation sequence. Sharp NanoSIMS profiles of $^{18}O$ at the $^{16}O$/$^{18}O$ interfaces indicate a dominant cationic diffusion at 800 and 900 °C, in agreement with the results obtained above by TEM-ASTAR characterizations. $^{18}O$-rich grains observed at the oxide/alloy interfaces imply a minor oxygen diffusion at grain boundaries. SIMS profiles of samples with a thin $^{54}Cr$ deposited layer also oxidized in Ar ($2\times10^{-5}$ atm) at 800 and 900 °C show a $^{54}Cr$-rich pic at the oxide/alloy interface, suggesting that the dominant cationic diffusion is via grain boundaries.

A comprehensive model is proposed to explain the experimental and numerical results obtained in the previous and present works: the growth of chromia at 500 and 900 °C is driven by the diffusion of oxygen vacancies and chromium vacancies, respectively.

## CRediT authorship contribution statement

**Xian Huang:** Conceptualization, Data curation, Formal analysis, Investigation, Visualization, Writing – original draft, Writing – review & editing. **Sophie Bosonnet:** Methodology, Validation, Writing – review & editing, Supervision. **Paul C. M. Fossati:** Validation, Writing – review & editing, Supervision. **Laurence Latu Romain:** Methodology, Validation, Writing – review & editing, Supervision. **Yves Wouters:** Validation, Writing – review & editing, Supervision. **Jérôme Aleon:** Methodology, Validation, Writing – review & editing. **Maximilien Verdier-Paoletti:** Methodology, Investigation, Writing – review & editing. **François Jomard:** Methodology, Investigation, Writing – review & editing. **Laure Martinelli:** Conceptualization, Methodology,

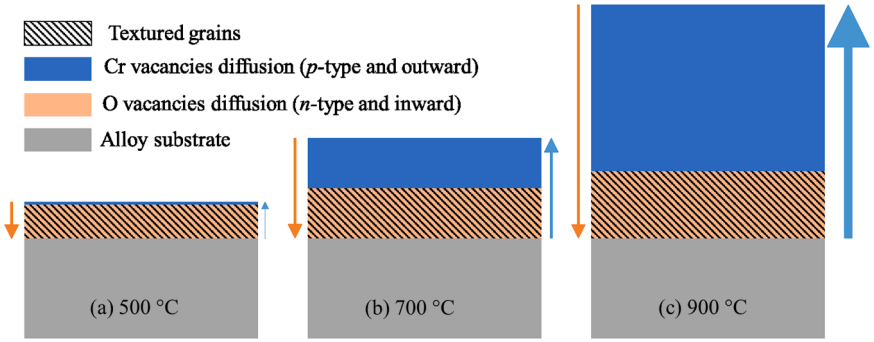


**Fig. 19.** Growth mechanisms of chromia oxide layer on Ni-30Cr at (a) low (500 °C), (b) intermediate (700 °C) and (c) high (900 °C) temperatures at an oxygen partial pressure from $5\times10^{-6}$ to $2\times10^{-5}$ atm. Chromia grown via Cr and O vacancy diffusion are marked in blue and orange, respectively. The alloy substrate is in grey. The hatched area is the textured grains along the *c*-axis of chromia near internal surface.

Writing – review & editing, Supervision, Project administration, Funding acquisition.

## Declaration of Competing Interest

The authors declare that they have no known competing financial interests or personal relationships that could have appeared to influence the work reported in this paper.

## Acknowledgements

The authors would like to thank the advice of Kevin Ginestar for oxidation tests and SEM, Jérôme Varlet for XRD, Anaïs Luangxay and Christophe Bonnet for thin-film deposition. The authors would like to thank the assistance of Gilles Renou for TEM-ASTAR, Larbi Sayah for quartz tube fabrication, Florence Robaut for SEM-FIB preparation.

## Appendix A: Oxidation tests with isotopic tracers

Oxidation tests with $^{18}O$ were performed either in a single-furnace thermobalance or in sealed quartz tube (Rhines pack [36]) in two separate furnaces. In the thermobalance, samples were oxidized in a mixed gas of Ar and Ar-1 %$O_2$ ($^{16}O_2$ or $^{18}O_2$) whose nominal oxygen partial pressure was $2\times10^{-5}$ atm measured before oxidation. The flows of argon and oxygen were controlled by mass flow meters to guarantee a total flow of 200 mL·min$^{-1}$ with fixed nominal oxygen partial pressure. Since the Ar gas may have a little residual $^{16}O_2$ gas and some $^{16}O_2$ gas may come from the environment via tube junctions, the $^{18}O$ enrichment in the oxidizing gas may not attain 100 % when performing tests with $^{18}O$.

In the Rhines pack, samples were placed on one end of the tube, while mixed powders, whose purpose was to fix the oxygen partial pressure within the tube, were placed at the other end. Both ends of the tube were heated by two separated furnaces so that the oxygen partial pressure in the Rhines pack could be adjusted by changing the temperature of the mixed powders without changing the oxidation temperature. The tube was filled with argon at approximately 0.25 bar at room temperature so that the total pressure was near 1 bar in the sealed tube at 900 °C. A mixture of $Cu_2O$ and CuO powders, whose oxygen partial pressure at thermodynamic equilibrium at 900 °C should be $2\times10^{-5}$ atm, was chosen to control the atmosphere in the tube. In principle, CuO is reduced to $Cu_2O$ after heating to release oxygen to maintain this equilibrium oxygen partial pressure at the temperature. After oxidation tests, the mixed powders were analysed by X-ray diffraction to verify the existence of CuO and $Cu_2O$ to guarantee that the equilibrium was held for the whole duration of the oxidation. To introduce $^{18}O$ in the atmosphere during the 1st oxidation, $Cu^{18}O_x^{16}O_{1-x}$ prepared by oxidizing $Cu_2^{16}O$ in $^{18}O_2$ was used for the mixed powders. Since residual $^{16}O_2$ gas may also be present when filling the tube with Ar before sealing and $^{16}O$ can be released by the mixed powder $Cu^{18}O_x^{16}O_{1-x}$ /$Cu_2^{16}O$, the $^{18}O$ enrichment in the oxidation environments should be lower in Rhines Pack than in thermobalance.

For tests performed with $^{54}Cr$ tracers, Pt was deposited directly on the surface of the alloy, without any protective layer formed by pre-oxidation. $^{54}Cr$ was deposited on one side of the samples and Pt spots were deposited on the other side. According to the SIMS analysis, the Pt markers diffused towards the alloy substrate during oxidation at 800 and 900 °C. The same phenomenon was observed in a sample on which gold markers were deposited, and which was subsequently oxidized at 500 °C, indicating that the formation of a thin protective layer is necessary before marker deposition in order to prevent the diffusion of the markers towards the substrate between 500 and 900 °C. The results of Pt marker experiments were therefore not considered in this study.

## Appendix B: Mixing-roughness-information depth model

The quantification of a SIMS profile is described by the mixing-roughness-information (MRI) depth model which is well summarized in the article by Hofmann [188]. In this model, the isotope content $N$ (in molar fraction) at the depth $x$ (in nm), estimated by the ratio between the count of an isotope and the total count of all isotopes, is proportional to the convolution product of the depth distribution $X$ and the depth resolution $g$:

$$N(x) = X(x) * g(x) = \int_{-\infty}^{+\infty} X(x)g(x'-x)dx' \,. \tag{1}$$

The depth resolution function has three contributions: the atomic mixture $g_w$, the depth of information $g_\lambda$ and the roughness of the abraded surface $g_\sigma$:

$$g = g_w * g_\lambda * g_\sigma \tag{2}$$

$$g_w(x) = \frac{1}{w}\exp\left(-\frac{x+w}{w}\right)u(x+w) \tag{3}$$

$$g_\lambda(x) = \frac{1}{\lambda}\exp\left(\frac{x}{\lambda}\right)u(-x) \tag{4}$$

$$g_\sigma(x) = \frac{1}{\sigma\sqrt{2\pi}}\exp\left(-\frac{x^2}{2\sigma^2}\right) \tag{5}$$

where $w$, $\lambda$ and $\sigma$ are respectively the characteristic length (in nm) for the atomic mixture function, information depth function and the surface roughness function, and $u$ is the step function.

For a parametric study, we consider a gate function centred at the origin with a gate width of 400 nm as the depth distribution function. Fourier and inverse Fourier transforms are used in order to easily compute the convolution. For the atomic mixing effect, caused by the $Cs^+$ or $O^-$ ion beam that penetrates the substrate matrix during SIMS measurement, the characteristic length can be estimated by an ion bombardment simulation in the SRIM software. In this simulation, chromia is bombarded by 104 $Cs^+$ ions with an energy of 15 keV and at an incident angle of 27°, the conditions that were used in the SIMS measurements in this study. Most of the ions stop at a longitudinal depth of 6.8 nm. The depth of information is considered extremely small, around1 nm, since the intensities measured by SIMS come from atoms sputtered at the extreme surface. Surface roughness can vary greatly depending on initial polishing and on additional roughness induced by oxidation. Fig. 20 shows the calculated profiles for the parametric study. The

default atomic mixture (6.8 nm) and information depth (1 nm) do not significantly change the shape of gate, while a roughness of 50 nm already greatly changes the shape of the gate function.

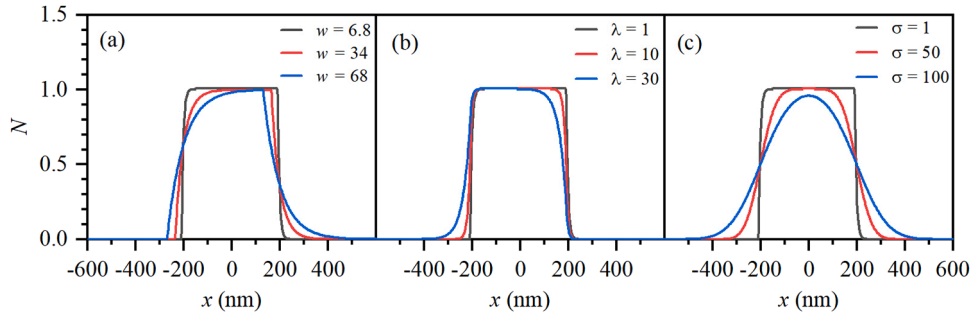


**Fig. 20.** Profile of $N$ at the depth $x$ calculated by the MRI model for a parametric study on (a) the characteristic length of the atomic mixture $w$, (b) the depth of information $\lambda$ and (c) the surface roughness $\sigma$. The default settings (in nm) are $w = 6.8$, $\lambda = 1$ and $\sigma = 1$.

According to the above parametric study, the atomic mixture and information depth effects can be neglected under the experimental conditions used in this study. Consequently, their functions reduce to a Dirac function. Using a step function centred at the origin for the depth distribution of the isotope, the expression of isotope content becomes:

$$N(x) = \frac{N_+ + N_-}{2} + \frac{N_+ - N_-}{2}\,\mathrm{erf}\left(\frac{x}{\sqrt{2}\,\sigma}\right) \tag{6}$$

where $N_-$ and $N_+$ are the content of the isotope before and after the step, respectively.

To compare, the volume diffusion between two semi-infinite mediums results in the equation:

$$N(x) = \frac{N_+ + N_-}{2} + \frac{N_+ - N_-}{2}\,\mathrm{erf}\left(\frac{x}{2\sqrt{Dt}}\right) \tag{7}$$

where $D$ is the diffusion coefficient of isotope in $nm^2 \cdot s^{-1}$ and $t$ the diffusion time in s.

The similarity between Eq. (6) and Eq. (7) suggests that SIMS measurements on a mirror surface of samples after diffusion (during a time interval $t$ with a diffusion coefficient $D$) could obtain the same profiles as on a rough surface (roughness $\sigma = \sqrt{2Dt}$) of samples without diffusion. Table 3 shows the volume diffusion coefficient and roughness fitted with the NanoSIMS and SIMS profiles of $^{18}O$ tracers measured in this study. Roughness measurements by profilometer are carried out on samples oxidized at 800 and 900°C, and the arithmetic roughness (Ra) are about 250 and 400 nm, respectively. These values are higher than those in Table 3 obtained by fitting the SIMS profiles, highlighting the influence of the roughness on the profiles. A mirror surface with roughness $\sigma \leq \sqrt{2Dt}$ is then necessary for fitting the diffusion coefficient from SIMS profiles.

**Table 3**
Coefficient of volume diffusion of O $D_{O,vol}$ and surface roughness $\sigma$ fitted with SIMS profiles of Ni-30Cr oxidized sequentially in $^{18}O$ and then in $^{16}O$.

| Temperature (°C) | Oxidation time in $^{16}O$ (h) | $D_{O,vol}$ ($cm^2 \cdot s^{-1}$) | $\sigma$ (nm) |
|---|---|---|---|
| 800 | 150 | $9.2 \pm 0.7 \times 10^{-17}$ | $100 \pm 4$ |
| 900 | 75 | $7.0 \pm 1.6 \times 10^{-16}$ | $194 \pm 23$ |

## Appendix C. Supporting information

Supplementary data associated with this article can be found in the online version at doi:10.1016/j.corsci.2024.112585.

## Data Availability

Data will be made available on request.

## References

[1] F. Cattant, D. Crusset, D. Féron, Corrosion issues in nuclear industry today, Mater. Today 11 (2008) 32–37, https://doi.org/10.1016/S1369-7021(08)70205-0.
[2] K.L. Murty, I. Charit, Structural materials for Gen-IV nuclear reactors: challenges and opportunities, J. Nucl. Mater. 383 (2008) 189–195, https://doi.org/10.1016/j.jnucmat.2008.08.044.
[3] S.J. Zinkle, G.S. Was, Materials challenges in nuclear energy, Acta Mater. 61 (2013) 735–758, https://doi.org/10.1016/j.actamat.2012.11.004.
[4] A. Atkinson, Transport processes during the growth of oxide films at elevated temperature, Rev. Mod. Phys. 57 (1985) 437–470, https://doi.org/10.1103/RevModPhys.57.437.
[5] L. Bataillou, C. Desgranges, L. Martinelli, D. Monceau, Modelling of the effect of grain boundary diffusion on the oxidation of Ni-Cr alloys at high temperature, Corros. Sci. 136 (2018) 148–160, https://doi.org/10.1016/j.corsci.2018.03.001.
[6] L. Bataillou, L. Martinelli, C. Desgranges, S. Bosonnet, K. Ginestar, F. Miserque, Y. Wouters, L. Latu-Romain, A. Pugliara, A. Proietti, D. Monceau, Growth kinetics and characterization of chromia scales formed on Ni–30Cr alloy in impure argon at 700 °C, Oxid. Met. 93 (2020) 329–353, https://doi.org/10.1007/s11085-020-09958-7.
[7] X. Huang, L. Martinelli, S. Bosonnet, P.C.M. Fossati, L. Latu-Romain, Y. Wouters, Effect of temperature on the oxidation mechanism of Ni-30Cr alloy, Oxid. Met. 96 (2021) 69–80, https://doi.org/10.1007/s11085-021-10049-4.
[8] D.J. Young, High Temperature Oxidation and Corrosion of Metals, 1st ed, Elsevier, Oxford, UK, 2008. ⟨https://www.elsevier.com/books/high-temperature-oxidation-and-corrosion-of-metals/young/978-0-08-044587-8⟩.
[9] C.S. Giggins, F.S. Pettit, The oxidation of TD NiC (Ni-20Cr-2 vol pct $ThO_2$) between 900° and 1200°C, Metall. Trans. 2 (1971) 1071–1078, https://doi.org/10.1007/BF02664238.
[10] T.A. Ramanarayanan, R. Petkovic-Luton, Investigations on the growth mechanisms of α-$Cr_2O_3$ on Ni-base alloys with and without $Y_2O_3$ dispersions, Ber. Bunsenges. F.

üR. Phys. Chem. 89 (1985) 402–409, https://doi.org/10.1002/bbpc.19850890409.
[11] T.A. Ramanarayanan, R. Ayer, R. Petkovic-Luton, D.P. Leta, The influence of yttrium on oxide scale growth and adherence, Oxid. Met. 29 (1988) 445–472, https://doi.org/10.1007/BF00666845.
[12] E. Schmucker, C. Petitjean, L. Martinelli, P.-J. Panteix, S.B. Lagha, M. Vilasi, Oxidation of Ni-Cr alloy at intermediate oxygen pressures. I. Diffusion mechanisms through the oxide layer, Corros. Sci. 111 (2016) 474–485, https://doi.org/10.1016/j.corsci.2016.05.025.
[13] G.M. Ecer, G.H. Meier, Oxidation of high-chromium Ni-Cr alloys, Oxid. Met. 13 (1979) 119–158, https://doi.org/10.1007/BF00611976.
[14] G.A. Hope, I.M. Ritchie, The oxidation of thin chromium films, Thin Solid Films 34 (1976) 111–114, https://doi.org/10.1016/0040-6090(76)90145-0.
[15] K.P. Lillerud, P. Kofstad, On high temperature oxidation of chromium: I. Oxidation of annealed, thermally etched chromium at 800°-1100°C, J. Electrochem. Soc. 127 (1980) 2397–2410, https://doi.org/10.1149/1.2129478.
[16] S.C. Tsai, A.M. Huntz, C. Dolin, Diffusion of $^{18}O$ in massive Cr2O3 and in Cr2O3 scales at 900°C and its relation to the oxidation kinetics of chromia forming alloys, Oxid. Met. 43 (1995) 581–596, https://doi.org/10.1007/BF01046900.
[17] S.C. Tsai, A.M. Huntz, C. Dolin, Growth mechanism of $Cr_2O_3$ scales: oxygen and chromium diffusion, oxidation kinetics and effect of yttrium, Mater. Sci. Eng. A 212 (1996) 6–13, https://doi.org/10.1016/0921-5093(96)10173-8.
[18] L. Bataillou, Modélisation de l'oxydation à haute température des alliages Ni-Cr, Université de Toulouse, 2019.
[19] M.J. Graham, J.I. Eldrige, D.F. Mitchell, R.J. Hussey, Anion transport in growing $Cr_2O_3$ scales, Mater. Sci. Forum 43 (1989) 207–242, https://doi.org/10.4028/www.scientific.net/MSF.43.207.
[20] C. Poulain, A. Seyeux, S. Voyshnis, P. Marcus, Volatilization and transport mechanisms during Cr oxidation at 300 °C studied in situ by ToF-SIMS, Oxid. Met. 88 (2017) 423–433, https://doi.org/10.1007/s11085-017-9756-y.
[21] L. Latu-Romain, Y. Parsa, S. Mathieu, M. Vilasi, M. Ollivier, A. Galerie, Y. Wouters, Duplex *n*- and *p*-Type chromia grown on pure chromium: a photoelectrochemical and microscopic study, Oxid. Met. 86 (2016) 497–509, https://doi.org/10.1007/s11085-016-9648-6.
[22] L. Latu-Romain, Y. Parsa, S. Mathieu, M. Vilasi, A. Galerie, Y. Wouters, Towards the growth of stoichiometric chromia on pure chromium by the control of temperature and oxygen partial pressure, Corros. Sci. 126 (2017) 238–246, https://doi.org/10.1016/j.corsci.2017.07.005.
[23] L. Latu-Romain, Y. Parsa, M. Ollivier, S. Mathieu, M. Vilasi, G. Renou, F. Robaut, Y. Wouters, About the control of semiconducting properties of chromia: investigation using photoelectrochemistry and orientation mapping in a TEM, Mater. High. Temp. 35 (2018) 159–167, https://doi.org/10.1080/09603409.2017.1389113.
[24] Y. Parsa, L. Latu-Romain, Y. Wouters, S. Mathieu, T. Perez, M. Vilasi, Effect of oxygen partial pressure on the semiconducting properties of thermally grown chromia on pure chromium, Corros. Sci. 141 (2018) 46–52, https://doi.org/10.1016/j.corsci.2018.06.038.
[25] J. Stringer, B.A. Wilcox, R.I. Jaffee, The high-temperature oxidation of nickel-20 wt % chromium alloys containing dispersed oxide phases, Oxid. Met. 5 (1972) 11–47, https://doi.org/10.1007/BF00614617.
[26] A.M. Huntz, S.C. Tsaï, J. Balmain, K. Messaoudi, B. Lesage, C. Dolin, Atomic transport in $Cr_2O_3$ and $Al_2O_3$ scales: growth mechanism and effect of Yttrium, Mater. Sci. Forum 251–254 (1997) 313–324, https://doi.org/10.4028/www.scientific.net/MSF.251-254.313.
[27] G. Hultquist, E. Hörnlund, Q. Dong, Platinum-induced oxidation of chromium in $O_2$ at 800 °C, Corros. Sci. 45 (2003) 2697–2703, https://doi.org/10.1016/S0010-938X(03)00117-3.
[28] Q. Dong, G. Hultquist, G.I. Sproule, M.J. Graham, Platinum-catalyzed high temperature oxidation of metals, Corros. Sci. 49 (2007) 3348–3360, https://doi.org/10.1016/j.corsci.2007.03.010.
[29] F. Czerwinski, On the use of the micromarker technique for studying the growth mechanism of thin oxide films, Acta Mater. 48 (2000) 721–733, https://doi.org/10.1016/S1359-6454(99)00396-1.
[30] L. Latu-Romain, T. Roy, T. Perez, Y. Parsa, L. Aranda, R. Podor, S. Mathieu, M. Vilasi, Y. Wouters, Should gold marker or TEM-ASTAR characterization be used to determine oxide growth direction? Oxid. Met. 96 (2021) 201–211, https://doi.org/10.1007/s11085-021-10042-x.
[31] H. Falk-Windisch, P. Malmberg, M. Sattari, J.-E. Svensson, J. Froitzheim, Determination of the oxide scale growth mechanism using $^{18}O$-tracer experiments in combination with Transmission Electron Microscopy and nanoscale Secondary Ion Mass Spectrometry, Mater. Charact. 136 (2018) 128–133, https://doi.org/10.1016/j.matchar.2017.12.001.
[32] K.P.R. Reddy, J.L. Smialek, A.R. Cooper, $^{18}O$ Tracer studies of $Al_2O_3$ scale formation on NiCrAl alloys, Oxid. Met. 17 (1982) 429–449, https://doi.org/10.1007/BF00742122.
[33] S.N. Basu, J.W. Halloran, Tracer isotope distribution in growing oxide scales, Oxid. Met. 27 (1987) 143–155, https://doi.org/10.1007/BF00667055.
[34] X. Huang, L. Martinelli, S. Bosonnet, P.C.M. Fossati, L. Latu-Romain, Y. Wouters, Chromium depletion in a Ni-30Cr alloy during high-temperature oxidation, High. Temp. Corros. Mater. 100 (2023) 745–773, https://doi.org/10.1007/s11085-023-10198-8.
[35] E.F. Rauch, M. Véron, Automated crystal orientation and phase mapping in TEM, Mater. Charact. 98 (2014) 1–9, https://doi.org/10.1016/j.matchar.2014.08.010.
[36] F.N. Rhines, A metallographic study of internal oxidation in the alpha solid solutions of copper, Trans. Metall. Soc. AIME 137 (1940) 246–286.
[37] M. Verdier-Paoletti, Etude des conditions physique et chimique de l'altération hydrothermale dans les astéroïdes carbonés de type C, Theses, Museum national d'histoire naturelle - MNHN PARIS; Centre de recherches pétrographiques et géochimiques (Vandoeuvre-lès-Nancy, Meurthe-et-Moselle), 2017. ⟨https://tel.archives-ouvertes.fr/tel-01948886⟩.
[38] F.A. Stevie, Secondary Ion Mass Spectrometry: Applications for Depth Profiling and Surface Characterization, Momentum Press, New York, NY, 2016.
[39] S.M. Daiser, C. Scholze, J.L. Maul, The checkerboard technique: an essential progress in SIMS data acquisition and evaluation, Nucl. Instrum. Methods Phys. Res. Sect. B Beam Interact. Mater. At. 35 (1988) 544–549, https://doi.org/10.1016/0168-583X(88)90328-X.
[40] J. Zurek, D.J. Young, E. Essuman, M. Hänsel, H.J. Penkalla, L. Niewolak, W.J. Quadakkers, Growth and adherence of chromia based surface scales on Ni-base alloys in high- and low-$pO_2$ gases, 3rd Int. Conf. Spray Depos. Melt At. SDMA 2006 6th Int. Conf. Spray Form. ICSF VI 477 (2008) 259–270. https://doi.org/10.1016/j.msea.2007.05.035.
[41] Y. Xie, T.D. Nguyen, J. Zhang, D.J. Young, Corrosion behaviour of Ni-Cr alloys in wet $CO_2$ atmosphere at 700 and 800 °C, Corros. Sci. 146 (2019) 28–43, https://doi.org/10.1016/j.corsci.2018.10.029.
[42] T.D. Nguyen, J. Zhang, D.J. Young, Silicon contamination during alloy oxidation in water vapour at 650 °C, Oxid. Met. (2022), https://doi.org/10.1007/s11085-022-10108-4.
[43] S. Hofmann, From depth resolution to depth resolution function: refinement of the concept for delta layers, single layers and multilayers, Surf. Interface Anal. 27 (1999) 825–834, https://doi.org/10.1002/(SICI)1096-9918(199909)27:9<825::AID-SIA638>3.0.CO;2-D.
[44] C. Wagner, Equations for transport in solid oxides and sulfides of transition metals, Prog. Solid State Chem. 10 (1975) 3–16, https://doi.org/10.1016/0079-6786(75)90002-3.
[45] A. Atkinson, Grain-boundary diffusion: an historical perspective, J. Chem. Soc. Faraday Trans. 86 (1990) 1307, https://doi.org/10.1039/ft9908601307.
[46] A. Atkinson, R.I. Taylor, The diffusion of $^{63}$ Ni along grain boundaries in nickel oxide, Philos. Mag. A 43 (1981) 979–998, https://doi.org/10.1080/01418618108239506.
[47] A. Suzuki, Y. Mishin, Atomic mechanisms of grain boundary diffusion: low versus high temperatures, J. Mater. Sci. 40 (2005) 3155–3161, https://doi.org/10.1007/s10853-005-2678-0.
[48] D. Chen, J. Wang, T. Chen, L. Shao, Defect annihilation at grain boundaries in alpha-Fe, Sci. Rep. 3 (2013) 1450, https://doi.org/10.1038/srep01450.
[49] S. Starikov, M. Mrovec, R. Drautz, Study of grain boundary self-diffusion in iron with different atomistic models, Acta Mater. 188 (2020) 560–569, https://doi.org/10.1016/j.actamat.2020.02.027.
[50] K.P. McKenna, A.L. Shluger, First-principles calculations of defects near a grain boundary in MgO, Phys. Rev. B 79 (2009) 224116, https://doi.org/10.1103/PhysRevB.79.224116.
[51] W. Körner, P.D. Bristowe, C. Elsässer, Density functional theory study of stoichiometric and nonstoichiometric ZnO grain boundaries, Phys. Rev. B 84 (2011) 045305, https://doi.org/10.1103/PhysRevB.84.045305.
[52] P. Heitjans, J. Kärger, Diffusion in Condensed Matter, Springer, Berlin, Heidelberg, 2005, https://doi.org/10.1007/3-540-30970-5.
[53] L. Latu-Romain, S. Mathieu, M. Vilasi, G. Renou, S. Coindeau, A. Galerie, Y. Wouters, The role of oxygen partial pressure on the nature of the oxide scale on a NiCr model alloy, Oxid. Met. 88 (2016) 481–493, https://doi.org/10.1007/s11085-016-9670-8.
[54] P. Kofstad, T. Norby, Defect Transp. Cryst. Solids (2007).
[55] X. Huang, P.C.M. Fossati, L. Martinelli, S. Bosonnet, L. Latu-Romain, Y. Wouters, A DFT study of defects in paramagnetic $Cr_2O_3$, Phys. Chem. Chem. Phys. 24 (2022) 10488–10498, https://doi.org/10.1039/D1CP05756A.